

UC Berkeley

UC Berkeley Previously Published Works

Title

Exploring microstructures in lower mantle mineral assemblages with synchrotron x-rays

Permalink

<https://escholarship.org/uc/item/4904q8g5>

Journal

Science Advances, 7(1)

ISSN

2375-2548

Authors

Chandler, Brian
Bernier, Joel
Diamond, Mathew
[et al.](#)

Publication Date

2021

DOI

10.1126/sciadv.abd3614

Peer reviewed

GEOPHYSICS

Exploring microstructures in lower mantle mineral assemblages with synchrotron x-rays

Brian Chandler^{1,2*}, Joel Bernier³, Mathew Diamond¹, Martin Kunz², Hans-Rudolf Wenk¹

Understanding dynamics across phase transformations and the spatial distribution of minerals in the lower mantle is crucial for a comprehensive model of the evolution of the Earth's interior. Using the multigrain crystallography technique (MGC) with synchrotron x-rays at pressures of 30 GPa in a laser-heated diamond anvil cell to study the formation of bridgmanite [(Mg,Fe)SiO₃] and ferropericlasite [(Mg,Fe)O], we report an interconnected network of a smaller grained ferropericlasite, a configuration that has been implicated in slab stagnation and plume deflection in the upper part of the lower mantle. Furthermore, we isolated individual crystal orientations with grain-scale resolution, provide estimates on stress evolutions on the grain scale, and report {110} twinning in an iron-depleted bridgmanite, a mechanism that appears to aid stress relaxation during grain growth and likely contributes to the lack of any appreciable seismic anisotropy in the upper portion of the lower mantle.

INTRODUCTION

The prevailing assumption is that the lower mantle (660 to 2900 km depth) is composed mostly of (Mg,Fe)SiO₃ bridgmanite (*br*) and (Mg,Fe)O ferropericlasite (*fp*). We understand little, however, regarding the intergranular microstructure and spatial distribution of these phases as well as their evolution under the thermomechanical conditions of the lower mantle by means of plastic deformation, phase transitions, and recrystallization. Of particular interest are the regions in the vicinity of sinking oceanic lithosphere, referred to as “slabs.” Seismic studies show increased anisotropy of seismic waves in and around subducting slabs, where the increased strain may induce plastic deformation and crystal preferred orientation (*1*), while the remaining mantle appears to be void of noticeable anisotropy. Furthermore, tomography studies have provided evidence that certain subduction systems, such as those of Tonga, Mariana, and Java (*2*), appear to stagnate around a depth of 500 to 1000 km in the upper portion of the lower mantle (*3*), while others penetrate down to the core-mantle boundary. A recent hypothesis (*4*) attributes the stagnation to a “viscosity hill” caused by an interconnected network of the less abundant (~20% by volume) *fp* around the volumetrically dominant *br*. In that study, an increase in strength in *fp* with increasing depth leads to about two orders of magnitude increase in viscosity around slabs, which could lead to stagnation and spreading.

Exploring the contribution of mineral properties to these phenomena has largely relied on x-ray diffraction techniques on powders using diamond anvil cells (DACs) combined with increasingly sophisticated laser heating methods to bring minerals to the conditions of the full range of the Earth's pressure-temperature conditions (*5–8*). Ex situ methods such as transmission electron microscopy (TEM) (*9*) have also been used, which provide increased resolution but must be performed at ambient conditions and generally use analog materials (*10*) that may take the same structure as minerals deep within the Earth but have different chemistry and properties. Although these techniques have laid the groundwork for understanding the structure and properties of lower mantle constituents, they lack the

mesoscale resolution (spanning 1 to 100 μm) (*11*) required to investigate multiphase aggregates in situ during dynamic events, such as phase transitions and recrystallization. The multigrain crystallography technique (MGC) (*12, 13*) adapted for use with DACs and combined with high-energy synchrotron x-ray facilitates the tracking of aggregates of hundreds of individual grains subject to thermomechanical processing. This method was successfully combined with powder diffraction to explore crystal orientations and grain behavior across the wadsleyite-to-ringwoodite transition of the mantle transition zone (*14, 15*) and used for in situ lattice parameter refinement and phase identification at the megabar pressures of the deeper lower mantle (*16, 17*). In this study, we use the “far-field” variant of MGC (*18, 19*) to investigate the evolution of intergranular microstructures and stress distributions within an orthorhombic (*Pnma*) San Carlos olivine (Mg_{0.88}Fe_{0.12})SiO₄ single crystal as it undergoes the high *P-T* dissociation reaction into cubic (*Cm3m*) *fp* and orthorhombic (*Pnma*) *br* at 30 GPa. This investigation provides the first grain-scale observation of the intergranular dynamics and crystalline relationships across this key transition.

RESULTS

Synchrotron x-ray diffraction experiments were conducted on each sample at a pressure of 30 GPa (corresponding to roughly 800-km depth) in two separate experiments. Experiment 1 was conducted on beamline 12.2.2 [$\lambda = 0.41329$, spot diameter of 15 μm at full width at half maximum (FWHM) using a PerkinElmer area detector positioned at a distance of 284 mm] at the Advanced Light Source (ALS) of Lawrence Berkeley National Laboratory. Experiment 2 was conducted on beamline 16-IDB High Pressure Collaborative Access Team (HPCAT) sector 16 ($\lambda = 0.40663$ spot size, 6 μm by 8 μm at FWHM) at the Advanced Photon Source (APS) of Argonne National Laboratory (ANL) using a MarCCD detector at a distance of 183 mm. In both experiments, the x-ray beam was initially focused on a CeO₂ powder standard to calibrate the two-dimensional (2D) detector parameters followed by calibration in three-dimensions (3D) using a 100-μm-diameter National Institute of Standards and Technology single-crystal ruby sphere (SRM 1990).

Single crystals extracted from a naturally occurring San Carlos olivine with composition (Mg_{0.88}Fe_{0.12})SiO₄ were selected as the starting material. Two cylindrical sections of 100 μm diameter by 50 μm

Copyright © 2021
The Authors, some
rights reserved;
exclusive licensee
American Association
for the Advancement
of Science. No claim to
original U.S. Government
Works. Distributed
under a Creative
Commons Attribution
NonCommercial
License 4.0 (CC BY-NC).

¹Department of Earth and Planetary Science, University of California, Berkeley, CA 94720, USA. ²The Advanced Light Source, Lawrence Berkeley National Laboratory, Berkeley, CA 94720, USA. ³Engineering Technologies Division, Lawrence Livermore National Laboratory, Livermore, CA 94551, USA.

*Corresponding author. Email: socm12@berkeley.edu

height were isolated from the same grain and loaded into a rhenium gasket preindented to the sample height and enclosed within a DAC. Three to five 5- μm -diameter ruby spheres were placed symmetrically on the sample chamber edge to monitor the pressure. Pressures before and after both experiments were found to be 30 ± 1.15 GPa. No pressure medium was used because of the intent of inducing plastic deformation in olivine before transforming to $br + fp$ at higher P/T for monitoring of any transformation texture that may occur.

The DAC containing the primary sample was aligned on the x-ray beam (ω) in transmission geometry and then rotated around an axis perpendicular to the x-ray beam (Fig. 1). After compression at ambient temperature, samples in both experiments were heated using a double-sided laser heating system. The sample in experiment 1 was heated at a temperature range of 1800 - 2000 K in four cycles (15, 30, 45, and 45 min), while in experiment 2, after the first heating cycle of 30 min, also conducted at 1800 to 2000 K, the temperature was increased to 2200 to 2600 K for the final three cycles of 60 min each to induce further grain growth in the br and fp phases. After each heating cycle, the sample was quenched to room-temperature and rotational series-diffraction images were collected with a detector mounted perpendicular to the x-ray beam at high pressure over a contiguous range ($\Delta\omega = 60^\circ, [-30^\circ 30^\circ]$) (Fig. 1). The diffracted x-ray intensities were integrated over successive steps of $\delta\omega = 0.25^\circ$, yielding image series with 240 individual frames for each dataset collected, which is then combined into a single aggregate diffraction image with each recorded intensity identified by its detector coordinates (2θ , η , and ω). Diffraction spots were assigned (indexed) to individual grains and refined using the HEXRD software package under the formalism provided in (18), which also allows for the identification individual grain orientation matrices and elastic strain tensor components leading to determination of average weighted centroids for grains.

Diffraction spot assignment proceeds by comparing theoretical diffraction spot locations based on input reference lattice parameters and corresponding cell symmetry with the measured spot locations in all three angular detector components (2θ , η , and ω) (figs.

S1, S2, and S4 and tables S1 and S2) representing the Bragg, azimuthal, and sample rotational angles, respectively. Trial orientations that satisfy a minimum ratio (completeness ratio) of observed to predicted reflections that meet all angular tolerances for a unique set of reciprocal lattice vectors (h , k , and l) are identified as grains. Those orientations are then used to assign the remaining observed reflections. A spot is only assigned once it meets all angular tolerances and predicted x - y locations on the detector face. Once a spot is assigned, it is removed to prevent reassignment. In several experiments, we have found that the angular thresholds are strongly detector dependent as is the completeness thresholding used in the trial orientation search. For example, in experiment 1, using the PerkinElmer area detector, initial completeness thresholds for both phases were set to a minimum of 40%, whereas in experiment 2, using an MarCCD, an initial completeness threshold of up to 70 to 80% was achievable.

To determine the orientation of the starting sample, in experiment 1, before compression, an initial dataset was obtained, which revealed two slightly misaligned olivine grains (misorientation of 6.91° ; fig. S2). The two unique orientations could clearly be seen by eye because of the spot doubling in the diffraction images (identified by arrows in fig. S2A) and most likely resulted from the sample fracturing during cell loading and/or cell closure. The starting sample orientation(s) in experiment 2 was not determined because of plastic deformation in the olivine, which occurred during DAC closure. However, we note that the initial olivine orientations in experiment 1 appear unrelated to newly formed br and fp orientations due to the dissociative nature of the phase transition.

Initial compression in both experiments leads to extensive plastic deformation expressed by streaking diffractions (column 1, fig. S3), which was annealed after the first heating cycle in experiment 2 but was somewhat retained throughout experiment 1. Complete conversion to $br + fp$ within the irradiated section was achieved after the third heating cycle of experiment 1 and the second in experiment 2. The phase transformation was accompanied by the appearance of several dispersed large diffracting centers and numerous near continuous rings of smaller diffractions (Fig. 2 and fig. S3, columns 2 to 4), indicating the emergence of two different grain morphologies. Figure 2A shows an ω -projected aggregated diffraction image taken after the second heating cycle of experiment 2 after subtraction of background detector noise, highlighting only reflections arising from the sample and diamond anvils. It is key to note that no distortion of diffraction spots occurred along the azimuth (η), indicating little to no activation of plastic deformation and most likely a pure grain nucleation condition. This observation also highlights the ability to track the evolution of individual intensities and shape of spots arising from individual grains, an ability that becomes increasingly powerful during experiments when the pressure step application can be controlled to allow for direct observation of the onset of yielding and which lattice plane(s) yield first as well as estimates of the relative size of each grain.

The different space groups and unit cell parameters for br (orthorhombic) and fp (cubic) facilitate the simultaneous identification and separation of grains of each phase (Fig. 2B). We identified a maximum of 48 individual br grains in any given dataset with 16 to 55 reflections per grain and constrained well enough to gain estimates of center of mass coordinates as well as the strain within the grain (table S2). Furthermore, we consistently observed several hundred grains of fp with 7 to 19 reflections per grain but found that only an average of ~ 80 provided enough reflections for estimates on

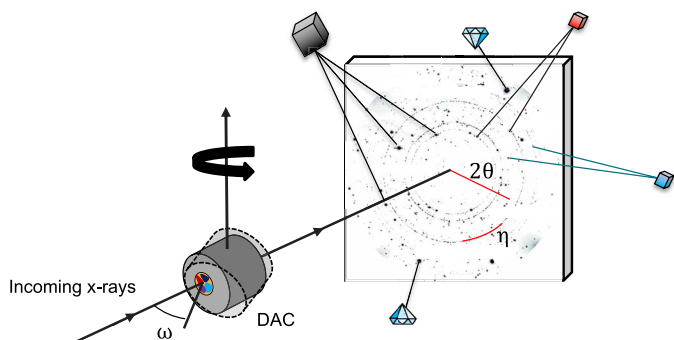


Fig. 1. Schematic of the experimental setup showing the “spotty” Debye-Scherrer rings that typify multigrain crystallography measurements. The spotty rings result when a relatively small number of distinctly oriented grains comprise the diffracting volume (black, red, and blue shapes). The detector image shows the projection of all 240 frames in the ω 0° to 60° rotation series. Each crystallite in the sample volume contributes a discrete subset of the observed reflection spots as do the diamond anvils (depicted by diamond symbols). Each distinct Bragg condition manifests as an intensity peak at the coordinates (2θ , η , and ω); 2θ is the Bragg angle converted from the radial distance to the beam center; η is the azimuth along the Debye-Scherrer ring.

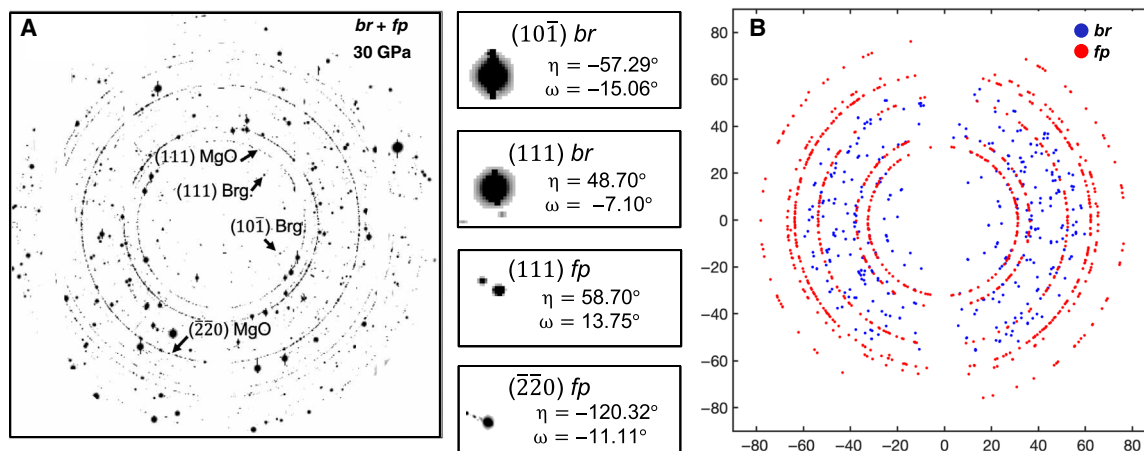


Fig. 2. Identification and separation of *br* and *fp* diffraction spots at 30 GPa. (A) Projection of 240 diffraction images following the phase transition in experiment 2 after background subtraction. Arrows indicate the locations of two reflections belonging to a single *br* and *fp* grain. Middle inset shows zoomed-in views of the selected diffraction peaks from (A), highlighting their compact Gaussian character after heating, indicating no observable plastic deformation in those grains. Note that the *fp* peaks are much smaller and numerous than the *br*, reflecting a much higher number yet small size of *fp* grains in the diffraction volume (B).

grain position and strain. The high symmetry and small lattice parameter of *fp* compared with *br* and the fact that only a fraction of the sample volume was in the beam during the rotation is a key limitation in the number of observable reflections. Moreover, intense reflections from the diamond anvils limited the usable data to 24° in the 2θ direction of each image, and intense reflections from the gasket material in experiment 1 due to the larger beam size greatly reduced the ability to identify *fp*. The grain orientations, however, are still well determined in both experiments. Initial peak searches were performed using the lattice parameters for *br* and *fp* (7). After indexation and convergence on the best-fit lattice parameters, these newly obtained values became the reference for the subsequent datasets. Figure 2B and figs. S4 and S5 show the 2θ and η coordinates for the measured diffraction spots assigned to grains from both phases in experiment 2 with blue denoting *br* having refined lattice parameters $a = 4.6630(4)$, $b = 4.8281(4)$, and $c = 6.7128(4)$ Å, and red denoting *fp* with lattice parameter $a = 4.0752(4)$ Å. Lattice parameter refinement was performed on the four best-fit grains for each phase and then arithmetically averaged to obtain the reported value.

During heating, the populations of *br* and *fp* inside the sample chamber evolved differently. The number of distinct *br* grains detected with MGC decreased in both experiments with successive heating cycles, while the number of *fp* grains increased from ~ 100 to several hundred. What became clear is that the polycrystalline aggregates in both experiments contained fewer, albeit more intensely reflecting, *br* grains immersed in a matrix of smaller, and what would be found, less strained *fp* grains (Fig. 3A). A comparison of diffraction intensities of all identified *fp* grains between the first and last heating cycles also showed a slight decrease in the average intensities for reflections with the largest structure factors (10 and 12%) for hkl {220} and {111}, while an increase by 54% was seen in the strongest *br* reflection (004) where hkl indicates the Miller indices of the reflecting lattice plane.

Because of the increased detector resolution and x-ray brilliance provided in experiment 2, we were able to further spatially constrain the locations for 10 to 50 individual grains of both phases within the 100- μm -diameter sample chamber. These grains provide insight into the spatial distribution of phases within the sample chamber and estimates of the equivalent Von Mises stress and strain (Fig. 3A).

Having access to the full elastic strain tensor for each indexed grain allows us to obtain estimates of the stress within grains. To better constrain these values, we further isolated only those grains falling within a 100- μm distance from sample centroid location determined (table S2) during the initial 3D calibration in both experiments. This approach was taken due to the fact that solving the strain tensor for each grain consists of 12 variables: the 3 angular components of diffraction vector location, 3 grain center of mass components, and 6 strain tensor components through the methodology described in (18). Grains with well-constrained diffraction vector locations and grain center-of-mass locations with respect to the single-crystal calibration should provide the best constraints on the elastic strain tensor and, therefore, the stress. Elastic strain tensors (ϵ_{kl}) were then combined with estimates of the single-crystal elastic tensors (C_{ijkl}) for both *br* and *fp* (20, 21), which were rotated coincident with the crystal orientations obtained using MGC, allowing us to obtain direct estimates of the stress within the grains under the assumption of linear elasticity through the application of the Hooke's law $\sigma_{ij} = C_{ijkl}\epsilon_{kl}$. The Von Mises equivalent stress and strain were then calculated for each grain using Eqs. 1 and 2 (22) through a combination of the MTEX software package (23, 24) and custom-written postprocessing software.

$$\epsilon_{\text{eq}} = \frac{2}{3} \sqrt{\frac{(\epsilon_{11} - \epsilon_{22})^2 + (\epsilon_{22} - \epsilon_{33})^2 + (\epsilon_{11} - \epsilon_{33})^2 + 6(\epsilon_{12}^2 + \epsilon_{13}^2 + \epsilon_{23}^2)}{2}} \quad (1)$$

$$\sigma_{\text{eq}} = \sqrt{\frac{(\sigma_{11} - \sigma_{22})^2 + (\sigma_{22} - \sigma_{33})^2 + (\sigma_{11} - \sigma_{33})^2 + 6(\sigma_{12}^2 + \sigma_{13}^2 + \sigma_{23}^2)}{2}} \quad (2)$$

We find that with each heating cycle, the average equivalent stress of both phases decreased globally, with *fp* reaching a minimum of 3.26 GPa after the third cycle (Fig. 3B and table S3), while we observed an overall drop of 3.54 GPa in *br* between heating cycles 1 and 4. Both phases showed slight oscillations in the calculated stress (slight stair-step pattern in Fig. 3B), which can be explained by the iterative heating method inducing growth at different rates

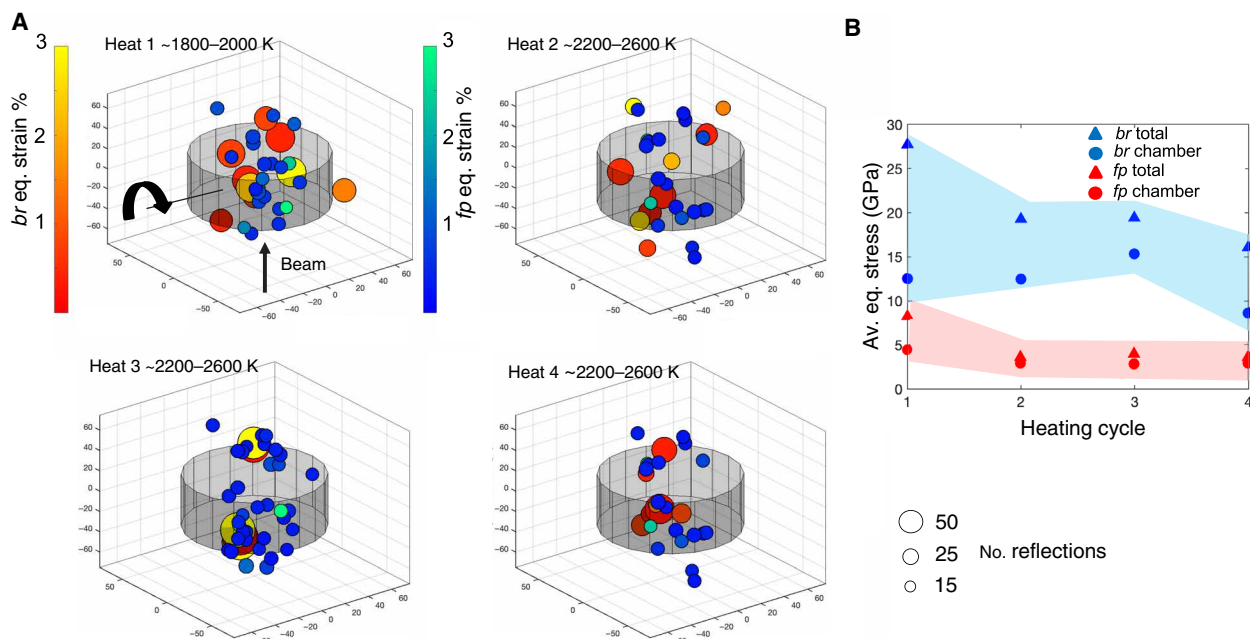


Fig. 3. Grain spatial and stress/strain distribution. (A) 3D distribution of *br* and *fp* grains constrained within the 100- μm radius from sample center after each heating cycles 1 to 4 in experiment 2. Dot sizes scaled by the number of reflections assigned to each grain (legend shown in lower right). Grain colors are in % equivalent elastic strain. (B) Average equivalent stress in *br* (blue) and *fp* (red) plotted against heating cycle for both phases showing the decreasing trend in stress with each heating cycle for all indexed grains (triangles) compared to those constrained to the sample chamber (circles). Black arrows represent incident beam direction and the rotational axis of the sample in (A). Along the beam direction remains the least constrained spatial coordinate due to limited DAC rotation angles.

accompanied with grain reorganization, which would bring different grains into better diffracting conditions with each cycle.

Recent studies have investigated the relative strengths of *br* and *fp* under a wide range of strain environments both experimentally and theoretically (25, 26), concluding that the softer *fp* phase accommodates most of the deformation. The samples, or model, in those studies were subject to conditions of substantial plastic deformation. By contrast, here, we observe strains imparted through grain growth and mismatched thermal expansion alone, as indicated by the Gaussian nature of the diffraction spots previously mentioned, which were maintained throughout the experiment. Our findings indicate that the *br* phase bears most of the elastic strain in this regime, $\sim 1.5\%$ average versus $\sim 0.5\%$ for *fp*, and is also more stressed by a factor of 2 and 3 (average ~ 9 to 14 GPa versus ~ 3 to 7 GPa for *fp*) (Fig. 3), which appears to emerge during grain growth and is followed by relaxation in a stepwise fashion with each consecutive heating cycle.

We are aware that a key influence of error in the elastic strain determination, and therefore, the stress calculation, comes from uncertainty in crystal lattice parameters and elastic parameters used and the limited scanning range due to x-rays being blocked by the cell body. It is expected that these limitations would lead to a scaling effect on the calculated equivalent stress values but not undermine the observed trends. This aspect is shown in Fig. 3B, which compares the average stress for grains with positions well constrained to the sample chamber compared to all identified grains. We find that nearly identical trends are observed with only a slight scaling affect where the poorer constrained set shows a higher stress value. This relationship leads us to conclude that values obtained for the best constrained set are most likely closer to an upper bound limit.

The spatial distribution of phases determined using MGC was visually confirmed by scanning electron microscopy (SEM) on the

sample recovered from experiment 2 where we performed both electron backscatter microscopy (BS-SEM) and energy-dispersive spectroscopy (EDS) (Fig. 4) on the recovered sample. Normally, SEM analysis of the recovered sample would only provide surface characterization; here, when removing the sample, the topmost layer remained with the diamond culet, which provided access to the sample subsurface that is visually estimated at 5 to 10 μm . The heated area of the sample exhibited several larger structures depleted of Fe and immersed in a matrix of smaller grains having high amounts of Fe-Mg but depleted of Si. Compositional analysis confirmed that these larger “grains” (1 to 12 μm) were *br*, while the finer-grained (<1 and 2 μm) network was *fp*, further endorsing the theory that *fp* likely forms an interconnected network around the larger stiffer *br* phases at experimental conditions corresponding to the lower mantle. We note that the observed disproportioning of Fe most likely occurs in the lower mantle, in agreement with density functional theory calculations, which modeled ferrous iron partitioning in *br* and *fp* phases at lower mantle conditions (27), as well as with studies conducted at higher pressures and similar temperatures (28, 29). The large-temperature gradients induced by the laser heating in our investigation are due to lack of insulation material and might exaggerate the experimentally observed extent. This implies that a fairly pure end-member form of *br* may be the most abundant in higher-temperature areas of the lower mantle.

The ensembles of respective crystal orientations determined for both phases provide the basis for examining the microstructural evolution across the olivine \rightarrow *br* + *fp* phase transition. We find good agreement with *br* and *fp* textures previously measured with the r-DAC using the powder method (Fig. 5) (5, 7). In experiment 1, we were able to assign diffraction spots and identify grains not only for *br* and *fp* but also for remaining metastable olivine.

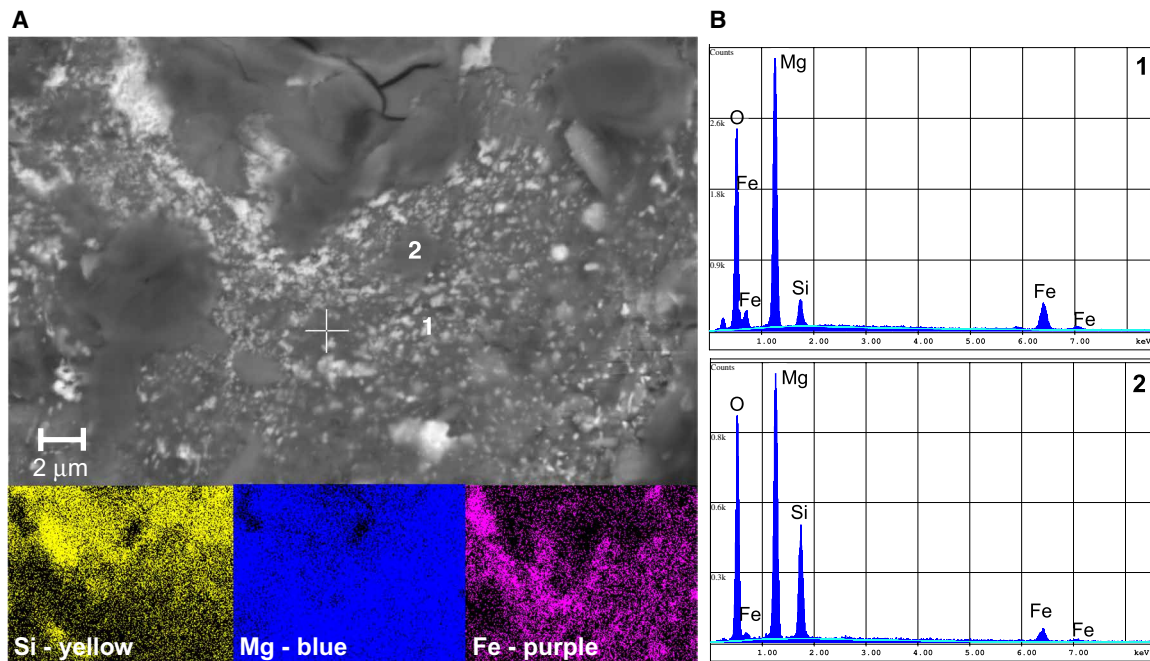


Fig. 4. SEM and EDS of decompressed recovered sample from experiment 2. (A) SEM backscatter electron image of sample within the laser heating spot and corresponding maps of Si (yellow), Mg (blue), and Fe (purple). Iron appears bright in SEM-BE image. (B) Spectra collected at two locations labeled 1 and 2 in (A).

Particularly, in experiment 1, there are *br* maxima (red intensities in Fig. 5) along the compression direction, extending from (001) to (100) in the inverse pole figures (IPFs) (Fig. 5, columns 4 and 5, rows 2 and 3) indicating that these lattice planes oriented toward the compression direction. While the transition from olivine may not be the natural path in the lower mantle, because of the intermediary phases wadsleyite and ringwoodite, the results show that we were able to sample the statistical bulk orientation distribution for the newly formed phases when inducing the transformation from a single crystal. Moreover, this version of MGC provides a straightforward route for studying intricate phase transition dynamics under extreme conditions, considering that maintaining good powder diffraction patterns becomes increasingly difficult at elevated temperatures due to the spotty nature of the diffraction patterns introduced by nucleation and recrystallization.

With successive heating cycles, the appearance of a notable pseudo-mirror symmetry appeared in the *br* IPF's (Fig. 5, column 4, rows 4 and 5) in both experiments, accompanied with a sharpening of maxima indicating grain coarsening, while the *fp* orientation distribution remained near random. We interpret this change in the distribution of *br* orientations, accompanied with a decrease in the number of detectable grains, as recrystallization and growth in the *br* phase.

Having direct access to each individual grain orientation allows us to investigate the origin of the newly formed *br* distribution directly. We began by isolating two separate pairs of maxima arising from two separate grains, shown in Fig. 5, row 5 (pair 1, orange circles; pair 2, white circles), followed by determining the spatial location within the sample chamber of the grains that gave rise to each of these isolated maxima (Fig. 6). Each associated pair of maxima was determined to originate from a unique pair of *br* orientations with overlapping grain centroids and parallel to the crystallographic *c* axes. The orientation relationship within each pair of grains was

found to be a 90° rotation about the *c* axis, effectively interchanging *a* and *b* axes and can be interpreted as {110} twins, which would act as a mechanism for relieving deviatoric strain. Each grain pair also consisted of one higher and one lower average equivalent stress grain (26.48 and 1.15 GPa, and 27.78 and 2.03 GPa), shown in Fig. 6 and the same image but from the perspective of the incident beam in fig. S5 showing grains lying along the incident beam axis, which was focused on the sample center.

DISCUSSION

Figures 5 and 6 demonstrate the various scales made accessible by far-field MGC. On the sample scale, the smaller (1 sub- μm), less strained *fp* appears to be distributed around the consistently larger (up to $\sim 10\ \mu\text{m}$) *br* grains in a configuration consistent with the formation of an interconnected network also seen in Fig. 4. Along these lines, the observed reduction in diffraction intensity of *fp* coupled with the increasing number of grains after each heating cycle is consistent with grain-size reduction. This effect is in agreement with the assumption that the viscosity in the upper portion of the lower mantle is affected by an interconnected *fp* network but in a slightly different way than described by Marquardt and Miyagi (4). The initial formation of the interconnected network of a weaker *fp* could act initially to decrease the viscosity around a penetrating slab, as proposed by Yamazaki and Karato (30), perhaps allowing complete or partial penetration beyond the 660-km depth. As the slab pushes through the surrounding mantle, leading to plastic deformation, the increase in strength in *fp* predicted by (4) would act to slow the slab due to the predicted increase in the surrounding viscosity. In addition to these effects, a scenario that arises from our findings is that when considering the observed diffraction intensity increase from *br* with each heating cycle, which implies grain growth, it is likely that the interconnected network of *fp* exists only over a finite depth

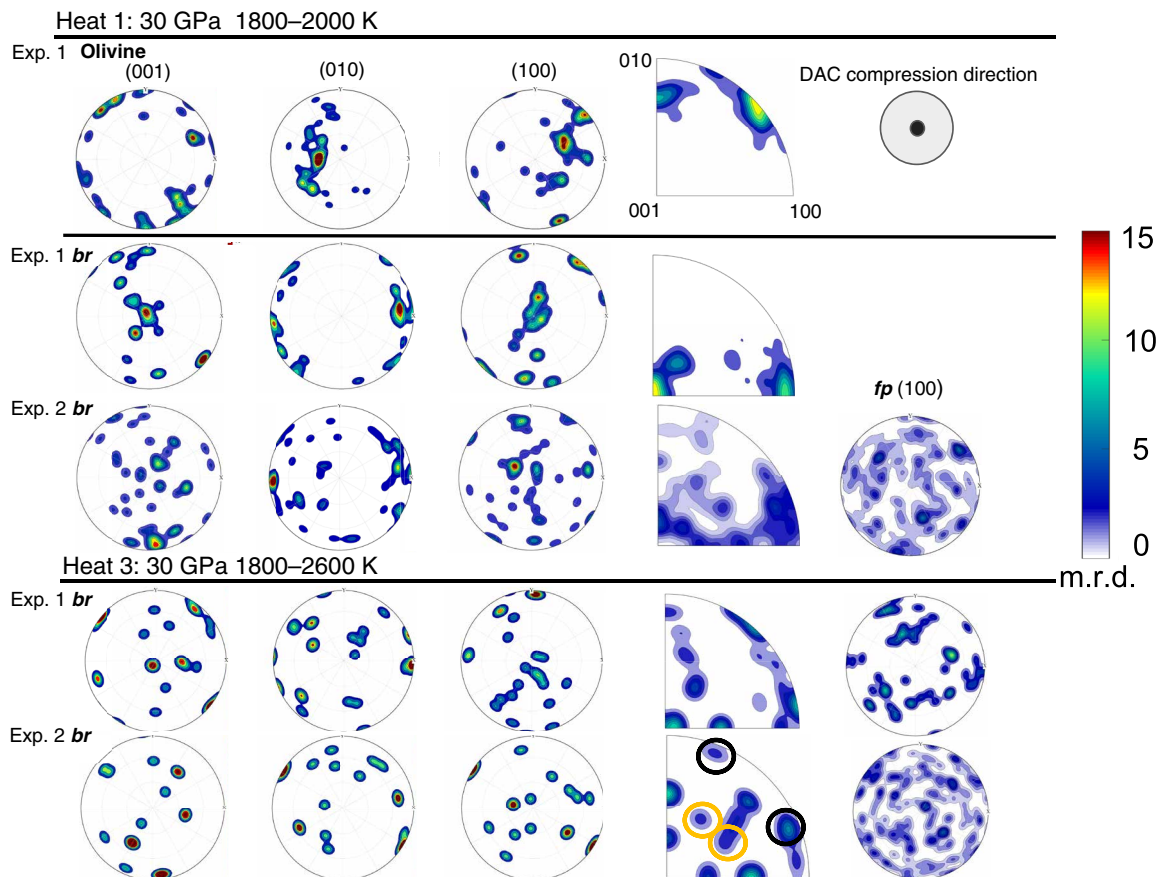


Fig. 5. Olivine and *br* and *fp* grain orientations from experiments 1 and 2 represented as PFs (columns 1 to 3 and 5) and IPFs (column 4). (Row 1) Olivine textures extracted from 49 unique orientations in experiment 1. (Rows 2 to 3) *br* textures retrieved from experiments 1 (15 grains) and 2 (48 grains) after the first heating cycle at 1800 to 2000 K. (Row 4) *br* textures (16 grains) after third heating cycle in experiment 1 at 1800 K. (Row 5) Experiment 2 (21 grains) at 2200 to 2600 K. Increasing from blue to red indicates concentration of lattice plane normals. White and orange circles in *br* inverse pole figure (IPF) in row 5 represent individual orientations used for further analysis described in the following section. Column 5 displays a consistently nearly random distribution of *fp* with (100) PFs. Units for PFs and IPFs are in multiples of random distribution (m.r.d.). PFs and IPFs were calculated and plotted using the MTEX (23, 24).

range. Once *br* has grown enough to disrupt the *fp* network, a rheological turnover would occur allowing the stiffer *br* phase to assume rheological control. This effect could lead to a compounded increase in the viscosity surrounding the slab and ultimately stagnation. The rate of disintegration of the *fp* network, and therefore the depth range, would directly depend on the mantle temperature. For instance, experiment 1 and the first runs of experiment 2 conducted at average mantle temperatures (1800 to 2000 K) may see this effect at deeper depths, while the latter runs of experiment 2 conducted under hot mantle conditions (2200 to 2600 K) would see it sooner due to the expedient growth of *br*. In either case, on the basis of these findings, we predict that eventually, *br* would grow enough to disrupt this network and shift the control over the local rheology from *fp* to *br*.

Yamazaki *et al.* (31) provided experimental evidence of an interconnected network of *fp* under similar conditions using a Kawai-type multi-anvil press, by estimating the dihedral angle of a *br* + *fp* aggregate. While our results are consistent with those findings, they report an increase in the connectivity of *fp* with increasing temperature and also small difference in the grain sizes between the two phases, both at odds with the current study. Key differences lie in the methods of sample preparation and heating technique. In that

study, crushed powders ($\sim 1 \mu\text{m}$) from a synthetically derived olivine sample were used. Using a powder would likely introduce different boundary conditions on grain growth and a multitude of nucleation sites and furthermore, a different stress and strain conditions imparted on individual grains leading to a different microstructural evolution. Furthermore, the resistive heating mechanism in that study provides a smoother increase in temperature (reported at $100^\circ\text{C}/\text{hour}$), whereas the laser heating used in this study creates a temperature shock to the desired temperature upon coupling with the material and can also introduce large-temperature gradients and fluctuations. For example, in experiment 1, because of the Gaussian nature of the heating spot, we observed a stable uniform hot spot ($\pm 10 \text{ K}$) of $\sim 20 \mu\text{m}$ diameter but a gradient of up to 500 K away from the hot spot. Furthermore, in both experiments, we experienced short fluctuations of $\pm 300 \text{ K}$ before achieving stability at the desired temperature. We attempted to minimize the influence of these effects by maintaining the incident x-ray spot size smaller than the uniform portion of the heating spot, although influence of thermal gradients on the collected data cannot be completely ruled out due to the rotational nature of the data collection procedure where, at large angles of the scan, one may sample areas where the gradient was present. Incorporating SEM analysis of recovered sample cross sections

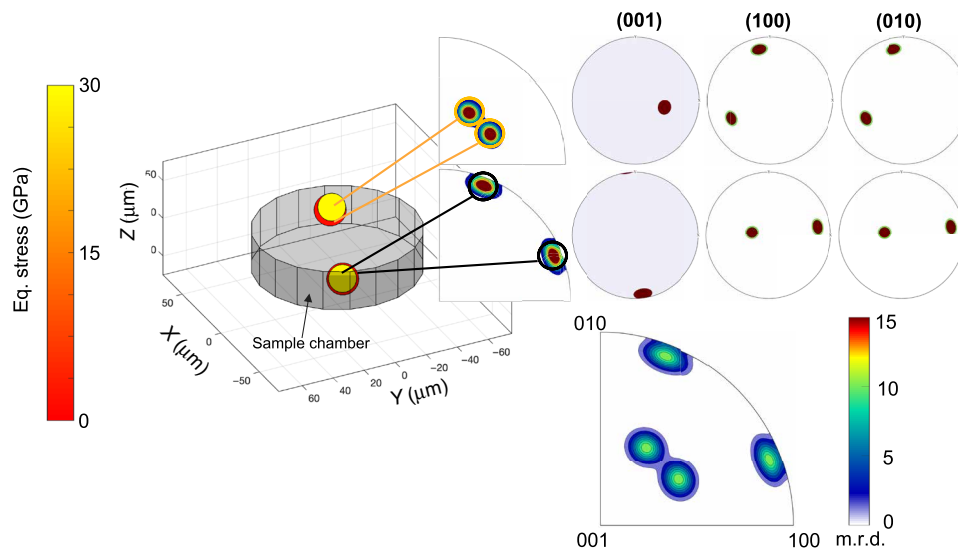


Fig. 6. Spatially resolved twinning relation observed in *br*. Two pairs (one pair indicated by orange circles, the other black in IPFs, highlighted in Fig. 5, fifth row) of *br* grain centroids, also shown at bottom (large). Grain color shows variation in average equivalent stress (GPa) with one high and one low stress grain in each pair located within the 100- μm -diameter sample chamber (labeled). (001) PFs (right) show single *c*-axis maxima in each pair indicative of {110} twinning. Units for pole PFs and IPFs are in m.r.d.

obtained via focused ion beam in future experiments would allow direct comparisons of microstructure between studies and also capture any effect due to temperature gradients from the laser heating. This approach would also allow for determination of the critical *br*/*fp* grain size ratio that would lead to the predicted rheological turnover due to disruption of the *fp* network.

Twinning in *br* has been the focus of multiple studies, Wang *et al.* (32) used ex situ TEM analyses of *br* synthesized under similar conditions (26 GPa and ~ 1870 K) and identified the same twinning relationship seen here, although it was attributed to stress relaxation during unloading. This is at odds with our findings and those of (33). In that study, twinning was observed in situ at high pressure, albeit indirectly through intensity analysis. In the present work, MGC allows us to directly observe this relation (Fig. 6) at in situ pressure with grain-scale resolution of spatial positions and stresses/strains in the parent/daughter pairs. While this twinning was also observed in *br* after extended heating in experiment 1, it occurred at a higher frequency in elevated temperature runs of experiment 2, where we found that after the fourth heating cycle, 48% of all identified *br* grains were twinned, compared to 24% after the fourth cycle in experiment 1. These findings coupled with the anisotropic nature of thermal expansion in *br* (34) lead us to infer that this is most likely a more energetically favorable way of deviatoric stress relaxation than plastic deformation by slip in *br* during grain growth across a large temperature range in the lower mantle as it was observed over the full experimental temperature range (1800 to 2600 K) conducted here. Furthermore, future explorations combining MGC with microbeam Laue diffraction (35) could provide a powerful combination and place further constraints on the stresses. Twinning could act to disperse crystal preferred orientation and it would therefore decrease any seismic anisotropy. When combined with the random distributions of *fp* found here, this would be consistent with a lower mantle void of any appreciable anisotropy (1) away from areas where increased plastic deformation occurs and crystal's preferred orientation develops.

While this study highlights a previously unexplored ability to capture mesoscopic information, spanning both the statistical orientation distribution and individual grain responses, the accuracy of the results is strongly dependent on several factors. Generally speaking, the orientations and magnitudes of deviatoric strain are not overly sensitive to factors like the quality of detector calibration and the instrument's stability. The measured centroidal positions and hydrostatic strains, however, are sensitive and thus more challenging to determine accurately (36). The size of the rotation range increases accuracy globally, as it leads to both more independent Bragg reflections and more variation in projection directions; this limitation is made apparent in the case of *fp* in this study, where after extended heating, hundreds of unique orientations were identified, but only a limited number could be constrained spatially. Achieving higher x-ray energies greatly increases refinement by granting a larger access to reciprocal space for a given detector distance. Another factor to consider is that, in these measurements, the x-ray beam only irradiated a small subvolume, ~ 6 to 16% of the total sample volume, during the scan, which cannot capture any large-scale heterogeneities that may exist or any variations in microstructures that may arise from temperature gradients near the sample edges due to the laser heating. Regardless, we have shown the ability to make direct in situ grain-scale observations of evolving microstructures and stress across phase transformations, a feat previously only captured through ex situ and statistical approaches. Furthermore, in a single experiment, we are able to gain estimates on the grain size, monitor growth, evolution of the stress environment of newly formed phases, as well as their spatial distribution, motivating a new route for exploring the complex behavior of materials under extreme conditions.

MATERIALS AND METHODS

Starting material and sample preparation

The starting sample material used in this study was extracted from a naturally occurring San-Carlos olivine with a composition of

(Mg_{0.88}Fe_{0.12})₂SiO₄, as confirmed by SEM/EDS analysis. A single section was removed from the hand sample and mounted to a glass slide using crystal bond and ground to a thickness of 50 μm. A single grain was then isolated from the petrographic thin section using polarized light microscopy based on the birefringence values for olivine. Two cylindrical sections with diameters of 100 μm and a height of 50 μm were removed from a select grain using the laser milling systems provided at each facility (ALS and HPCAT) using a laser power setting of 90% and performing 70 to 90 passes at a rate of 3 to 5 passes/s. No pretreatment of the samples was performed before or after removal of sections. Moreover, preparing samples intended for MGC with this method ensures sample homogeneity. An added advantage of this method is the Fe content of natural olivine, which couples well with infrared (IR) laser heating methods and prevents the need for any additional material in the sample chamber, which could complicate data analysis. We have tested several different sample preparation techniques when performing MGC (i.e., powders, grain chips, and crushed grains) to determine which method provides the best diffraction peak indexation results through maximizing the number of uniquely discernable diffraction spots arising from each target phase (i.e., generally the “spottiest” diffraction patterns). Therefore, when designing an experiment using MGC, the sample preparation technique is completely dependent on what information is desired. For this particular experiment, we have found that starting from a single crystal and then inducing the phase transformation provide better constraints on each of these parameters and even allow for the isolation of cubic *fp*, which, when starting from even a coarsened powder results in smooth diffraction rings that cannot be treated with MGC and also complicates the indexation process for other phases.

In both experiments, samples were loaded into a BX-90 DAC (37) with 90° opening angles. Two 300-μm culet Boehler-Almax diamonds were mounted on cubic boron nitride cBN seats, which are transparent to x-rays maximizing the availability of the accessible scanning range. In both experiments, a single sample cylinder was loaded into a preindented rhenium gasket that was laser drilled to match the sample size. Three- to 5-μm-sized ruby spheres were symmetrically placed on one diamond culet within the sample chamber to monitor the pressure in the cell before and after each scanning iteration. A pressure medium was not used because of the intent of inducing plastic deformation in the initial olivine before transforming to *br* + *fp* at higher *P/T* for monitoring of any transformation texture that may occur.

Laser heating

In both experiments, a double-sided heating technique was used. In experiment 1, performed at beamline 12.2.2 of the ALS (38), two 1090-nm IR fiber lasers were aligned coincident and focused to a 20-μm spot size onto both sides in the center of the sample, while the spot temperature was measured via a peak scaling technique from the spectrum collected by an Ocean Optics Jazz spectrometer. In experiment 2, conducted at beamline 16-IDB Sector 16 of HPCAT at APS, 1064-nm ytterbium fiber lasers were focused to a spot size of 20 μm on the center of the sample chamber. The temperature in experiment 2 was determined by fitting the Planck radiation function to the spectrum collected via a SP2560 Princeton spectrograph (39).

As far as the alignment of the heating lasers, in both experiments, we aligned the laser spots by visual alignment of the two hot spots (upstream and downstream) until they form one homogeneous hot

spot using the provided pyrometry imaging systems. We estimate the accuracy of the copositioning to be better than 20% of the diameter of the hot spot.

In experiment 1, for the first two heating runs, the heating laser was first focused near the sample center, and the coordinates were recorded. The sample was then translated in a circular pattern around the fixed beam location with intent to partially transform the heating area to explore any crystallographic relationship between the newly formed *br* and metastable olivine, although none was found. The resulting heating spot was also visually inspectable due to sample discoloration in the heated areas (darkening compared to the original transparent sample). By moving the heating spot only near the center of the sample chamber, we maximized the distance from the heated area to the location of the ruby spheres (roughly 30 to 40 μm of sample not directly heated) to prevent any interaction between the ruby spheres and the center of the sample. Furthermore, the incident x-ray spot size in both experiments was maintained smaller than the measured heating spot size, minimizing the effect of influence of temperature gradients in the scanned area. After the first two heating runs in experiment 1, the laser was refocused to the sample center where it remained for the third and fourth heating runs and was not translated. After each heating run, the x-ray beam was realigned to the coordinates of the sample center and a dataset was collected at the center of the sample chamber during after each heating run.

In experiment 2, the heating lasers were focused coincident on the sample center in the same fashion as in experiment 1, and the coordinates were recorded. Each heating cycle was performed at these coordinates, after which, the x-ray beam was brought coincident to these coordinates, ensuring that the dataset was collected at the same position. The same scanning position was used in each run to track the microstructural evolution of a single area throughout the experiment.

SUPPLEMENTARY MATERIALS

Supplementary material for this article is available at <http://advances.sciencemag.org/cgi/content/full/7/1/eabd3614/DC1>

REFERENCES AND NOTES

1. B. Romanowicz, H.-R. Wenk, Anisotropy in the deep Earth. *Phys. Earth Planet. Int.* **269**, 58–90 (2017).
2. Y. Fukao, M. Obayashi, Subducted slabs stagnant above, penetrating through, and trapped below the 660 km discontinuity. *J. Geophys. Res. Solid Earth* **118**, 5920–5938 (2013).
3. S. Widiyantoro, A. Gorbato, B. L. N. Kennett, Y. Fukao, Improving global shear wave traveltimes tomography using three-dimensional ray tracing and iterative inversion. *Geophys. J. Int.* **141**, 747–758 (2000).
4. H. Marquardt, L. Miyagi, Slab stagnation in the shallow lower mantle linked to an increase in mantle viscosity. *Nat. Geosci.* **8**, 311–314 (2015).
5. H.-R. Wenk, I. Lonardelli, S. Merkel, L. Miyagi, J. Pehl, S. Speziale, C. E. Tommaseo, Deformation textures produced in diamond anvil experiments, analyzed in radial diffraction geometry. *J. Phys. Condens. Matter* **18**, S933–S947 (2006).
6. H.-R. Wenk, L. Lutterotti, P. Kaercher, W. Kaniupanyacharoen, L. Miyagi, R. Vasin, Rietveld texture analysis from synchrotron diffraction images. II. Complex multiphase materials and diamond anvil cell experiments. *Powder Diffr.* **29**, 220–232 (2014).
7. L. Miyagi, H.-R. Wenk, Texture development and slip systems in bridgmanite and bridgmanite + ferropericlaes aggregates. *Phys. Chem. Miner.* **43**, 597–613 (2016).
8. A. E. Gleason, W. L. Mao, Strength of iron at core pressures and evidence for a weak Earth's inner core. *Nat. Geosci.* **6**, 571–574 (2013).
9. D. P. Dobson, N. Miyajima, F. Nestola, M. Alvaro, N. Casati, C. Liebske, I. G. Wood, A. M. Walker, Strong inheritance of texture between perovskite and post-perovskite in the D" layer. *Nat. Geosci.* **6**, 575–578 (2013).
10. F. Lin, M. Giannetta, M. Jugle, S. Couper, B. Dunleavy, L. Miyagi, Texture development and stress-strain partitioning in periclaes + halite aggregates. *Minerals* **9**, 679 (2019).

11. R. Pokharel, Overview of high-energy x-ray diffraction microscopy (HEDM) for mesoscale material characterization in three dimensions, in *Materials Discovery and Design*, T. Lookman, S. Eidenbenz, F. Alexander, C. Barnes, Eds. (Springer, Cham, 2018), *Springer Series in Materials Science*, vol. 280.
12. H. O. Sørensen, S. Schmidt, J. P. Wright, G. B. M. Vaughan, S. Teichert, E. F. Garman, J. Oddershede, J. Davaasambuu, K. S. Paithankar, C. Gundlach, H. F. Poulsen, Multigrain crystallography. *Zeitschrift für Kristallographie* **227**, 63–78 (2012).
13. H. F. Poulsen, S. Garbe, T. Lorentzen, D. J. Jensen, F. W. Poulsen, N. H. Andersen, T. Frello, R. Feidenhans'l, H. Graafsma, Applications of high-energy synchrotron radiation for structural studies of polycrystalline materials. *J. Synchrotron Rad.* **4**, 147–154 (1997).
14. A. D. Rosa, N. Hilaiet, S. Ghosh, G. Garbarino, J. Jacobs, J.-P. Perrillat, G. Vaughan, S. Merkel, *In situ* monitoring of phase transformation microstructures at Earth's mantle pressure and temperature using multi-grain XRD. *J. Appl. Cryst.* **48**, 1346–1354 (2015).
15. A. D. Rosa, N. Hilaiet, S. Ghosh, J.-P. Perrillat, G. Garbarino, S. Merkel, Evolution of grain sizes and orientations during phase transitions in hydrous Mg₂SiO₄. *J. Geophys. Res. Solid Earth* **121**, 7161–7176 (2016).
16. H. Yuan, L. Zhang, In situ determination of crystal structure and chemistry of minerals at Earth's deep lower mantle conditions. *Matter Radiat. Extremes* **2**, 117–128 (2017).
17. L. Zhang, D. Popov, Y. Meng, J. Wang, C. Ji, B. Li, H.-k. Mao, In-situ crystal structure determination of seifertite SiO₂ at 129 GPa: Studying a minor phase near Earth's core–mantle boundary. *Am. Mineral.* **101**, 231–234 (2016).
18. J. V. Bernier, N. R. Barton, U. Lienert, M. P. Miller, Far-field high-energy diffraction microscopy: A tool for intergranular orientation and strain analysis. *J. Strain Anal. Eng.* **46**, 527–547 (2011).
19. J. V. Bernier, R. M. Suter, A. D. Rollett, J. D. Almer, High-energy x-ray diffraction microscopy in materials science. *Ann. Rev. Mater. Res.* **50**, 395–436 (2020).
20. B. Wehinger, A. Bosak, S. Nazzareni, D. Antonangeli, A. Mirono, S. L. Chaplot, R. Mittal, E. Ohtani, A. Shatskiy, S. Saxena, S. Ghose, M. Krisch, Dynamical and elastic properties of MgSiO₃ perovskite (bridgmanite). *Geophys. Res. Lett.* **43**, 2568–2575 (2016).
21. H. Marquardt, S. Speziale, H. J. Reichmann, D. J. Frost, F. R. Schilling, Single-crystal elasticity of (Mg_{0.9}Fe_{0.1})O to 81 GPa. *Earth Planet. Sci. Lett.* **287**, 345–352 (2009).
22. A. F. Liu, *Mechanics and Mechanisms of Fracture: An Introduction* (ASM International, 2005).
23. F. Bachmann, R. Hielscher, H. Schaeben, Texture analysis with MTEX – Free and open source software toolbox. *Solid State Phenom.* **160**, 63–68 (2010).
24. D. Mainprice, R. Hielscher, H. Schaeben, Calculating anisotropic physical properties from texture data using the MTEX open-source package. *Geol. Soc. London Spec. Pub.* **360**, 175–192 (2011).
25. J. Girard, G. Amulele, R. Farla, A. Mohiuddin, S.-i. Karato, Shear deformation of bridgmanite and magnesiowüstite aggregates at lower mantle conditions. *Science* **351**, 144–147 (2016).
26. M. Kasemer, E. Zepeda-Alarcon, R. Carson, P. Dawson, H.-R. Wenk, Deformation heterogeneity and intragrain lattice misorientation in high strength contrast, dual-phase bridgmanite/periclaase. *Acta Mater.* **189**, 284–298 (2020).
27. J. M. R. Muir, J. P. Brodholt, Ferrous iron partitioning in the lower mantle. *Phys. Earth Planet. Int.* **257**, 12–17 (2016).
28. S.-H. Shim, B. Grocholski, Y. Ye, E. E. Alp, S. Xu, D. Morgan, Y. Meng, V. B. Prakapenka, Stability of ferrous-iron-rich bridgmanite under reducing midmantle conditions. *Proc. Natl. Acad. Sci. U.S.A.* **114**, 6468–6473 (2017).
29. L. Zhang, Y. Meng, W. Yang, L. Wang, W. L. Mao, Q.-S. Zeng, J. S. Jeong, A. J. Wagner, K. A. Mkhoyan, W. Liu, R. Xu, H.-k. Mao, Disproportionation of (Mg,Fe)SiO₃ perovskite in Earth's deep lower mantle. *Science* **344**, 877–882 (2014).
30. D. Yamazaki, S.-i. Karato, Some mineral physics constraints on the rheology and geothermal structure of Earth's lower mantle. *Am. Mineral.* **86**, 385–391 (2001).
31. D. Yamazaki, T. Yoshino, T. Matsuzaki, T. Katsura, A. Yoneda, Texture of (Mg,Fe)SiO₃ perovskite and ferro-periclaase aggregate: Implications for rheology of the lower mantle. *Phys. Earth Planet. Int.* **174**, 138–144 (2009).
32. Y. Wang, F. Guyot, A. Yeganeh-Haeri, R. C. Liebermann, Twinning in MgSiO₃ perovskite. *Science* **248**, 468–471 (1990).
33. J. Chen, D. J. Weidner, M. T. Vaughan, The strength of Mg_{0.9}Fe_{0.1}SiO₃ perovskite at high pressure and temperature. *Nature* **419**, 824–826 (2002).
34. N. Funamori, T. Yagi, W. Utsumi, T. Kondo, T. Uchida, M. Funamori, Thermoelastic properties of MgSiO₃ perovskite determined by in situ X-ray observations up to 30 GPa and 2000 K. *J. Geophys. Res. Solid Earth* **101**, 8257–8269 (1996).
35. H.-R. Wenk, B. C. Chandler, K. Chen, Y. Li, N. Tamura, R. Yu, Residual lattice strain in quartzites as a potential palaeo-piezometer. *Geophys. J. Int.* **222**, 1363–1378 (2020).
36. C. Langrand, N. Hilaiet, C. Nisr, M. Roskosz, G. Ribárik, G. B. M. Vaughan, S. Merkel, Reliability of multigrain indexing for orthorhombic polycrystals above 1 Mbar: Application to MgSiO₃ post-perovskite. *J. Appl. Cryst.* **50**, 120–130 (2017).
37. I. Kantor, V. Prakapenka, A. Kantor, P. Dera, A. Kurnosov, S. Sinogeikin, N. Dubrovinskaia, L. Dubrovinsky, BX90: A new diamond anvil cell design for x-ray diffraction and optical measurements. *Rev. Sci. Instrum.* **83**, 125102 (2012).
38. M. Kunz, J. Yan, E. Cornell, E. E. Domning, C. E. Yen, A. Doran, C. M. Beavers, A. Treger, Q. Williams, A. A. MacDowell, Implementation and application of the peak scaling method for temperature measurement in the laser heated diamond anvil cell. *Rev. Sci. Instrum.* **89**, 083903 (2018).
39. Y. Meng, R. Hrubak, E. Rod, R. Boehler, G. Shen, New developments in laser-heated diamond anvil cell with in situ synchrotron x-ray diffraction at High Pressure Collaborative Access Team. *Rev. Sci. Instrum.* **86**, 072201 (2015).

Acknowledgments: We thank A. Doran of ALS and M. Yue, J. G. Shen, J. Smith, and R. Hrubak of HPCAT for technical support. B.C. thanks S. Merkel for the constructive conversations during this work. This work was performed under the auspices of the U.S. Department of Energy (DOE) by Lawrence Livermore National Laboratory under contract DE-AC52-07NA27344. We appreciate comments from two anonymous reviewers that helped us to improve the manuscript. **Funding:** This research is supported by NSF (EAR 1343908 and CSEDI-106751) and DOE (DE-FG02-05ER15637). Portions of this work were performed at HPCAT (sector 16), APS, and ANL. HPCAT operations are supported by DOE-NNSA's Office of Experimental Sciences. The APS is a DOE Office of Science User Facility operated for the DOE Office of Science by ANL under contract no. DE-AC02-06CH11357. This research used resources of the Advanced Light Source, a U.S. DOE Office of Science User Facility under contract no. DE-AC02-05CH11231. B.C. was awarded an ALS doctoral fellowship to advance research using this technique, and this research is a part of Ph.D. thesis. M.D. was supported by the Carnegie/DOE Alliance Center (CDAC). The HEXRD software used in this study is available at <https://github.com/HEXRD/hexrd.git>. **Author contributions:** B.C. designed the study and performed the experiments and data analysis. J.B. provided the HEXRD software and assisted in its usage and data analysis. M.D. assisted in the experiment conducted at HPCAT of ANL. M.K. assisted with the laser heating and experimental considerations for the experiment conducted at ALS. H.-R.W. guided the progress of the experiment and assisted in result interpretation and writing the paper. B.C. wrote the paper, with feedback and contributions from all coauthors. All authors discussed and interpreted the results. **Competing interests:** The authors declare that they have no competing interests. **Data and materials availability:** All data needed to evaluate the conclusions in the paper are present in the paper and/or the Supplementary Materials. All experimental data and processing software are made available upon request.

Submitted 16 June 2020

Accepted 11 November 2020

Published 1 January 2021

10.1126/sciadv.abd3614

Citation: B. Chandler, J. Bernier, M. Diamond, M. Kunz, H.-R. Wenk, Exploring microstructures in lower mantle mineral assemblages with synchrotron x-rays. *Sci. Adv.* **7**, eabd3614 (2021).